JGR Earth Surface

RESEARCH ARTICLE
10.1029/2018JF004775

Calving Induced Speedup of Petermann Glacier

Martin Rückamp[1], Niklas Neckel[1], Sophie Berger[1,2], Angelika Humbert[1,3], and Veit Helm[1]

[1]Alfred Wegener Institute Helmholtz Centre for Polar and Marine Research, Bremerhaven, Germany, [2]Laboratoire de Glaciologie, Université libre de Bruxelles, Brussels, Belgium, [3]Department of Geosciences, University of Bremen, Bremen, Germany

Key Points:
- Based on remote sensing data, Petermann Glacier sped up after the calving event in 2012
- Speedup is caused by a reduction in buttressing
- Further retreat into the fjord likely causes glacier acceleration

Supporting Information:
- Supporting Information S1

Correspondence to:
N. Neckel and M. Rückamp,
niklas.neckel@awi.de;
martin.rueckamp@awi.de

Citation:
Rückamp, M., Neckel, N., Berger, S., Humbert, A., & Helm, V. (2019). Calving induced speedup of petermann glacier. *Journal of Geophysical Research: Earth Surface*, *124*, 216–228. https://doi.org/10.1029/2018JF004775

Received 29 MAY 2018
Accepted 18 DEC 2018
Accepted article online 11 JAN 2019
Published online 26 JAN 2019

Abstract This study assesses the response on ice dynamics of Petermann Glacier, a major outlet glacier in northern Greenland, to the 2012 and a possible future calving event. So far Petermann Glacier has been believed to be dynamically stable as another large calving event in 2010 had no significant impact on flow velocity or grounding line retreat. By analyzing a time series of remotely sensed surface velocities, we find an average acceleration of 10% between winter 2011/2012 and winter 2016/2017. This increase in surface velocity is not linear but can be separated into two parts, starting in 2012 and 2016 respectively. By conducting modeling experiments, we show that the first speedup can be directly connected to the 2012 calving event, while the second speedup is not captured. However, on recent remote sensing imagery newly developing fractures are clearly visible ~12 km upstream from the terminus, propagating from the eastern fjord wall to the center of the ice tongue, indicating a possible future calving event. By including these fracture zones as a new terminus position in the modeling domain, we are able to reproduce the second speedup, suggesting that surface velocities remain on the 2016/2017 level after the anticipated calving event. This indicates that, from a dynamical point of view, the terminus region has already detached from the main ice tongue.

1. Introduction

Draining ~4% of the Greenland ice sheet (Münchow et al., 2014), Petermann Glacier (PG) is one of the major outlet glaciers in northern Greenland. Being the second largest floating ice tongue in Greenland, it loses ice primary through bottom melting (80%) and secondary to surface losses and calving events (Falkner et al., 2011; Johnson et al., 2011; Rignot & Steffen, 2008). Several large calving events occurred in the past, but Petermann's terminus position was considered to be stationary between 1876 and 2010, that is, glacial readvance rates roughly equaled calving .on decadal time scales (Falkner et al., 2011). An outstanding calving event in August 2010 produced a large tabular iceberg with an area of 253 km^2 (Falkner et al., 2011), corresponding to 20% of the floating ice tongue as measured in January/February 2009 (Joughin & Moon, 2015). After 2 years of glacial readvance a second major calving event occurred in July 2012. Here another 147 km^2 was removed from the floating ice tongue, of which 124 km^2 started to drift as large tabular iceberg. By then, the remaining area of the floating ice tongue covered only 69% of the January/February 2009 extent. This terminus position marks the largest retreat since first measured in 1876 (Münchow et al., 2014). Since the 2012 calving event, PG has been steadily readvancing, but a newly developing fracture, from the eastern margin to the center of the ice tongue, marks a forthcoming calving event.

It is expected that these major calving events affect ice dynamics and hence ice discharge. As the fast-flowing floating tongue of PG is bounded by the lateral fjord sidewalls that exert a back stress on the glacier, a reduction in resistance or even a disintegration of the floating tongue could cause the glacier to speed up. A correlation between acceleration and calving has been observed at Jakobshavn Isbræ, the fastest marine-terminating outlet glacier of the Greenland ice sheet (Joughin et al., 2014). Although the mechanism that sustains glacier acceleration is not completely understood, the reduction of back stress is proposed to be the trigger of the observed speedup at Jakobshavn Isbræ (e.g., Bondzio et al., 2017).

The dynamic response of PG to the major calving event in August 2010 was investigated in detail by Nick et al. (2012). Based on remotely sensed surface velocities and 2-D flowline modeling, Nick et al. (2012) concluded that the 2010 calving event had no significant ice dynamical effect on PG. This is in line with

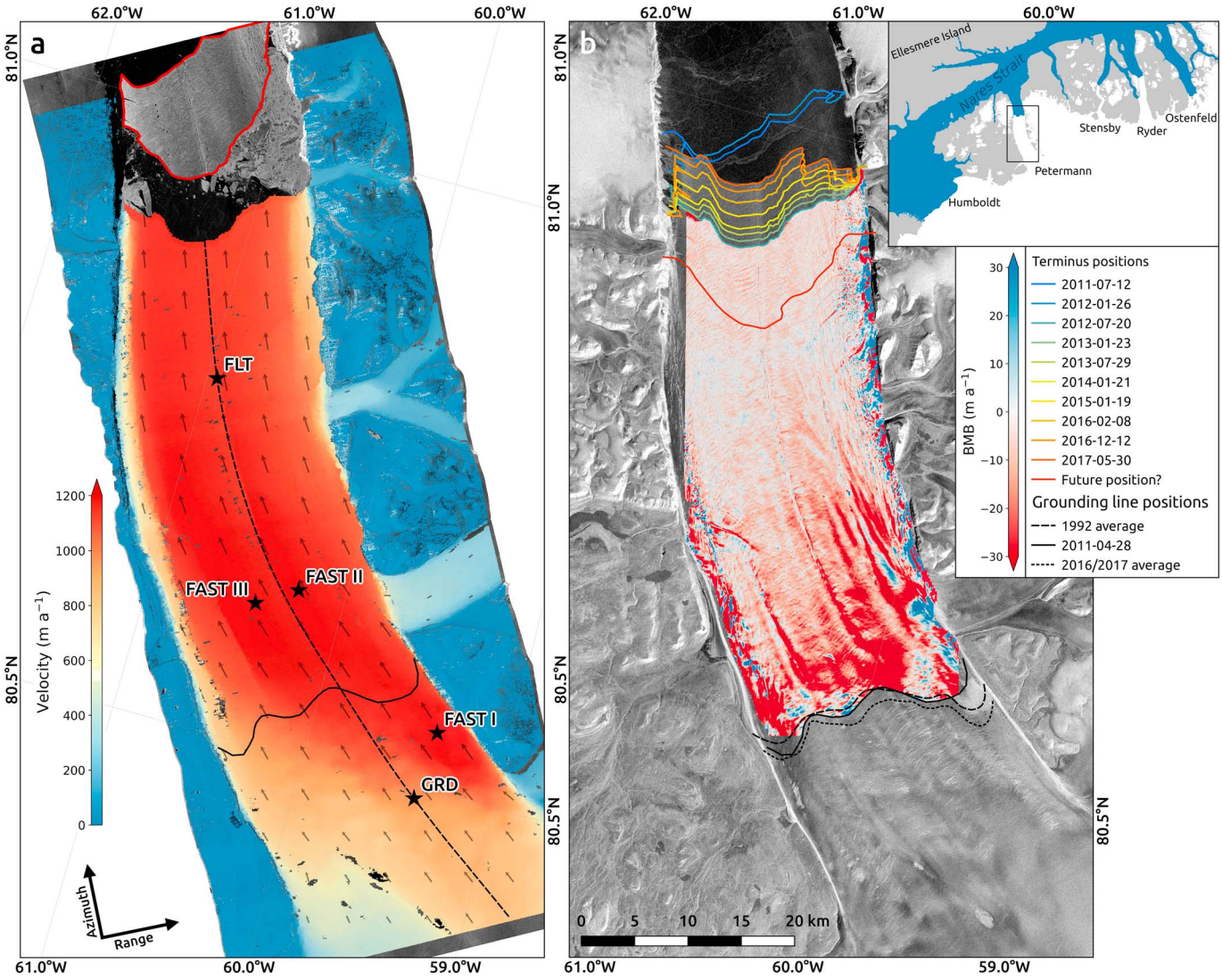

Figure 1. Surface velocities of Petermann Glacier for January 2013 are overlaid on a TerraSAR-X scene acquired on 20 July 2012. The 2012 iceberg is outlined in red (a). Terminus positions for the time period investigated in this study are shown on top of the 2012/2013 basal melt rates in a Lagrangian framework. Grounding line fluctuations from ERS-1/2 and Sentinel-1A/B Synthetic Aperture Radar interferometry are overlaid on top of a Sentinel-1B imagery acquired on 30 May 2017 (b).

the results from Hogg et al. (2016), who found no evidence of dynamic changes by observing grounding line positions between 1992 and 2011. Such a stability in ice dynamics contrasts with several other marine-terminating outlet glaciers in Greenland, for example, Helheim Glacier, Jakobshavn Isbræ, and Zachariæ Isstrøm, which showed significant acceleration after terminus retreat (Howat et al., 2005; Joughin et al., 2014; Mouginot et al., 2015). For PG, it has been suggested that its dynamic stability might be due to minor resistive forces in the 2010 terminus region (Nick et al., 2012). However, Nick et al. (2012) performed a subsequent retreat experiment where the calving front reaches deeper into the fjord, resulting in a larger velocity increase compared to their 2010 calving experiment. This might be a hint that the stability of the floating ice tongue is sensitive to the calving front position and accelerated terminus retreat.

In this study, we investigate the dynamic response of PG to the 2012 calving event. We based our analysis on remotely sensed surface velocities from TerraSAR-X and use ice flow modeling to investigate the causes of change. Observed velocity fields spanning from January 2012 to December 2016 are compared to simulated velocity fields for the same time period. We further extend the existing records of grounding line positions (e.g., Hogg et al., 2016) using Sentinel-1 Synthetic Aperture Radar (SAR) interferometry and update basal melt rates (e.g., Rignot & Steffen, 2008; Wilson et al., 2017) of PG in a Lagrangian framework by employing

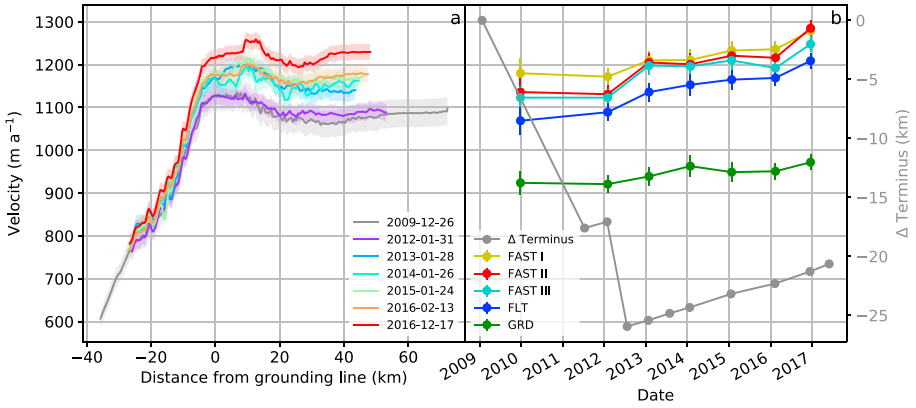

Figure 2. Time series of surface velocities along the central flowline shown in Figure 1a. Time series of surface velocities at 5 points shown in Figure 1. Point FLT is located on the floating tongue, point GRD is located on grounded ice, and points FAST I to FAST III are located in regions of high velocities. Next to surface velocities, terminus changes are shown relative to the winter 2008/2009 terminus position (b). The winter 2009/2010 (approximately 26 Decmeber 2009) surface velocity and the winter 2008/2009 (approximately 23 January 2009) terminus position are taken from the MEaSUREs data set (Joughin et al., 2010; 2015; Joughin & Moon, 2015).

high-resolution TanDEM-X surface elevations and surface mass balance estimates. In anticipation of a forthcoming calving event, we also estimate its potential impact on the ice dynamics of PG.

2. Observations

2.1. Surface Velocities

As PG is a *TanDEM-X Super Test Site*, several experimental TanDEM-X acquisitions are available. We selected an ascending satellite path covering the floating ice tongue within two satellite frames (Figure 1). Utilizing 11-day repeat pass acquisitions in December/January/February for the 2012–2016 time period, we calculated at least one velocity field for each winter with intensity offset tracking, employing 26 TanDEM-X acquisitions in total (Table S1 in the supporting information). In a first step, Single-Look Slant Range Complex data separated by 11 days were coregistered based on satellite orbit information and the Greenland Mapping Project digital elevation model (DEM; Howat et al., 2014). For each coregistered image pair, offsets in range and azimuth directions were calculated by cross correlating the backscatter intensity in predefined moving search windows (e.g., Strozzi et al., 2002). In this study, we chose a window size of 250 m in both range and azimuth direction, separated by a step size of 50 m. Range and azimuth offsets were translated into metric surface displacements and projected into a polar stereographic coordinate system with its origin at 90°N, 45°W and a standard parallel of 70°N. Velocity fields of each satellite frame were mosaiced by the corresponding satellite path and subsequently filtered following Lüttig et al. (2017).

Our error estimate for the TerraSAR-X surface velocities is based on the assumption that any surface movement on stable ground, that is, on exposed bedrock is erroneous. Therefore, we collected data points in these stable areas next to PG from each velocity field and estimated errors following Seehaus et al. (2015). When applying offset intensity tracking on high-resolution SAR data, not only horizontal motion can be observed but also the vertical movement in slant range between successive data acquisitions is measured (Joughin, Shean, Smith, & Dutrieux, 2016; Marsh et al., 2013). However, due to the lack of precise tidal measurements during the time of data acquisitions, we did not correct the velocities for tidal effects but assumed that the tidal-induced velocity error is only minor as the main flow direction of PG is in azimuth direction of the corresponding satellite path (Figures 1 and S1).

Figure 2a gives an overview of the time series of surface velocities along the central flow line shown in Figure 1a. In order to compare these estimates, we calculated average velocities along the profile. The velocities reach a maximum value of $1,135 \pm 18$ m a^{-1} in December 2016 and a minimum value of $1,031 \pm 31$ m a^{-1} in winter 2009/2010 (Joughin et al., 2010, 2015). The latter is very similar to our estimate of $1,037 \pm 21$ m a^{-1} in January/February 2012. This implies an average speedup of 10% between January/February 2012 and Dec 2016. As evident from Figure 2a the observed speedup is not advancing gradually but rather stepwise. From the profiles shown in Figure 2a we found an average acceleration of 49 and 40 m a^{-1} for the periods winter January/February 2012 to January 2013 and February 2016 to December

2016, respectively. Between January 2013 and February 2016 the observed variations in surface velocity did not exceed 12 m a^{-1}.

A similar pattern is observed when comparing individual locations in the velocity fields. For this we used the average value within a 1-km buffer around each point shown in Figure 1a. Maximum winter velocities are observed at location FAST II, reaching up to 1,285 ± 18 m a^{-1} in December 2016 (Figure 2b). At the same location surface velocities reach just 1,131 ± 21 m a^{-1} in January/February 2012, which is comparable to 1,136 ± 34 m a^{-1} as measured in winter 2009/2010, indicating an overall speedup of 14% between January/February 2012 and December 2016. From Figure 2b it becomes evident that, at this location, the first half of the observed speedup occurred between January/February 2012 and January 2013, while the second half occurred between February 2016 and December 2016. A similar behavior is found for locations FAST I and FAST III, but the overall speedup is less pronounced for location FAST I. Also at location GRD first signs of acceleration are found for the time period January/February 2012 to January 2013. A slightly different pattern is found for location FLT which already showed an acceleration of 20 m a^{-1} between winter 2009/2010 and January/February 2012.

2.2. Terminus Change

Changes in ice front location were estimated using the box measurement method as described by Moon and Joughin (2008). The size of the box was determined by the glacier margins and covers all terminus positions from 2009 to 2017. Terminus positions were manually delineated from TerraSAR-X and Sentinel-1B scenes acquired between 2011 and 2017 (Table S2). All data sets were processed from single-look complex data to multilooked and geocoded intensity imagery with a spatial resolution of 10 and 20 m for TerraSAR-X and Sentinel-1B, respectively. Additionally, we delineated a potential future terminus, following a large fracture reaching from the eastern fjord wall to the center of the floating tongue (Münchow et al., 2016; Figure S3). The initial box was split by each terminus position, and the seaward parts were removed. The area changes of the remaining boxes of two successive dates, divided by the box width, represent the average terminus retreat between the two dates (Table S2). Digitizing errors of terminus positions were estimated from repeated delineations of TerraSAR-X and Sentinel-1B scenes (Moon et al., 2015), leading to an average error of 8 m for TerraSAR-X and 23 m for Sentinel-1B.

Table S2 and Figure 2b give an overview of the terminus changes of PG between January/February 2009 and May 2017. In this time period PG showed its largest extent in January/February 2009, when the floating tongue measured an average length of 71 km. Between January/February 2009 and July 2011 the terminus retreated on average by 17.6 km before readvancing by 0.53 km until January 2012. The 2012 calving event resulted in an average terminus retreat of 8.87 km in the first half of 2012. Since then PG has gradually readvanced with an average rate of ∼1 km a^{-1}

2.3. Grounding Line Location

Grounding lines were located from SAR interferometry following well-established methods (e.g., Hogg et al., 2016; Rignot et al., 2011). Here we calculated 24 double differential interferograms for the years 1992, 2011, 2016, and 2017 from ERS-1/2 and Sentinel-1A/B data (Table S3). From all interferograms, we manually delineated the inland limit of tidal flexure, which is referred to as grounding line throughout this manuscript. For the years 1992 and 2016/2017 several coherent differential interferograms were derived; therefore, we were able to estimate an average grounding line position for these time periods (Figures 1b and S3). In order to quantify the variability of grounding line positions, we employed the box measurement method in a similar way to the terminus changes. The root-mean-square difference between the single grounding line positions and their respective average position leads to 437 and 362 m for the 1992 and 2016/2017 time period, respectively. However, in the most eastern part of PG, maximum variations in grounding line position can exceed these average values by up to 1 order of magnitude (Hogg et al., 2016; Figure S4). This implies that the average grounding line retreat, estimated with 1,356 and 1,195 m for 1992–2016/2017 and 2011–2016/2017, respectively, is not necessarily representative.

2.4. Basal Melt Rates

Basal melt rates were calculated using mass conservation in a Lagrangian framework as outlined in Berger et al. (2017). This method relies on mass conservation and deduces basal melting ($\dot{M}_b$; negative values for melting) by

$$\dot{M}_b = \frac{\mathrm{D}H}{\mathrm{D}t} + H\nabla \cdot \mathbf{v}_h - \dot{M}_s, \tag{1}$$

where $\dot{M}_s$ is the surface mass balance (positive values for accumulation), DH/Dt is the observed Lagrangian thickness change, H is the local ice thickness, and $\mathbf{v}_h = (u, v)$ is the horizontal velocity of the ice (see Berger et al., 2017 for more details). Ice thickness is obtained by hydrostatically inverting two TanDEM-X DEMs using ice and seawater densities of $\rho_i = 910\ \mathrm{kg\ m^{-3}}$ and $\rho_w = 1,027\ \mathrm{kg\ m^{-3}}$, respectively. Ellipsoidal elevations are converted to freeboard heights using the EGM 2008 geoid and the AOTIM5 tide model (Padman & Erofeeva, 2004). To correct for variations in firn and ice densities, firn-air content from RACMO 2.3 is used (Kuipers Munneke et al., 2015). The TanDEM-X DEMs are produced from single-pass bistatic SAR interferometry following Neckel et al. (2013). We calibrated and validated these DEMs with Operation IceBridge laser altimetry on surrounding rocky outcrops (Studinger, 2014) and present an accuracy better than 1 m on stable ground. Due to penetration of the SAR signal into snow, firn, and ice, these estimates might be biased on PG. However, considering the acquisition times of the DEMs and their location in the ablation zone of the Greenland ice sheet, penetration effects are assumed to be low (Wessel et al., 2016). The DEMs acquired on 20 July 2012 and 29 July 2013 (Table S1) are combined in a Lagrangian frame with a normalized cross correlation to produce one Lagrangian thickness change (and subsequent basal melting) field. Surface mass balance is cumulated over the respective time period from the 1 km downscaled RACMO 2.3 data set (Noël et al., 2016). Ice flow divergence is computed by combining the hydrostatic thickness fields with regularized TerraSAR-X velocity gradients (section 2.1 and Berger et al., 2017). After removing some noisy patches next to the fjord walls, the large-scale pattern of basal melt rates averages at 10.6 m $\mathrm{a^{-1}}$ and agrees well with previous estimates (Cai et al., 2017; Wilson et al., 2017). Highest melt rates >50 m $\mathrm{a^{-1}}$ are found in the grounding zone, and melting stays high in several channels which reach up to 20-km downstream (Figure 1b).

3. Numerical Ice Flow Modeling

3.1. Ice Flow Model

We use the Ice Sheet System Model (Larour et al., 2012) to model the ice dynamics and glacier geometry evolution of PG. The modeling domain covers the whole drainage basin (Zwally et al., 2012) up to the ice divides of PG (inset of Figure 3a). Model calculations are performed on an unstructured finite element grid with a high resolution of $l_{\mathrm{min}} = 0.2\mathrm{km}$ in fast-flowing regions (approximately >500 m $\mathrm{a^{-1}}$) and along small scale features such as the calving front; the interior obtaining a coarser resolution of $l_{\mathrm{max}} = 20\mathrm{km}$. In order to capture fractures on the floating tongue, these regions were refined with a mesh resolution of 0.02 km. In total, the mesh comprises about 86 000 elements (the mesh is illustrated in Figure S5).

Except in the area of the floating tongue, glacier geometry is taken from the mass conserving bed from BedMachine Greenland (Morlighem et al., 2014). On the floating tongue, the high-resolution pre-2012 calving ice surface from this study and the bathymetry from Bamber et al. (2013) are nested in the BedMachine v2 data set. Ice thickness and ice base are simply derived from the ice surface by employing the floating condition. The bathymetry under the floating tongue is poorly constrained due to lacking data coverage. However, this is not of crucial importance as the observations do not show large grounding line migration within the interested time period. When interpolating the geometry data sets to the numerical grid, the floating-grounded ice mask obtained from the floatation criterion differs from floating-grounded ice mask in Morlighem et al. (2014) at some locations. Therefore, we manually adjusted the ice thickness and bathymetry to match the mask in Morlighem et al. (2014). Additionally, we updated the mask in Morlighem et al. (2014) with the main grounding line and calving front positions of April 2011 and January 2012, respectively (obtained from this study; see Figure 1).

The ice flow is approximated with the Shelfy-Stream Approximation (SSA; MacAyeal, 1989) within a 2-D plan view model, which is appropriate for fast-flowing ice streams and ice shelf flow like PG. Basically, the SSA neglects vertical shearing, so that the flow equation is independent of z and a two-dimensional (2-D) model with two unknowns (the horizontal velocities u and v)

$$\frac{\partial}{\partial x}\left(4H\eta\frac{\partial u}{\partial x}+2H\eta\frac{\partial v}{\partial y}\right)+\frac{\partial}{\partial x}\left(H\eta\frac{\partial u}{\partial y}+H\eta\frac{\partial v}{\partial x}\right)=\rho_i g H\frac{\partial z_s}{\partial x}+\tau_{b,x}, \tag{2}$$

$$\frac{\partial}{\partial y}\left(4H\eta\frac{\partial v}{\partial y}+2H\eta\frac{\partial u}{\partial x}\right)+\frac{\partial}{\partial y}\left(H\eta\frac{\partial u}{\partial y}+H\eta\frac{\partial v}{\partial x}\right)=\rho_i g H\frac{\partial z_s}{\partial y}+\tau_{b,y}, \tag{3}$$

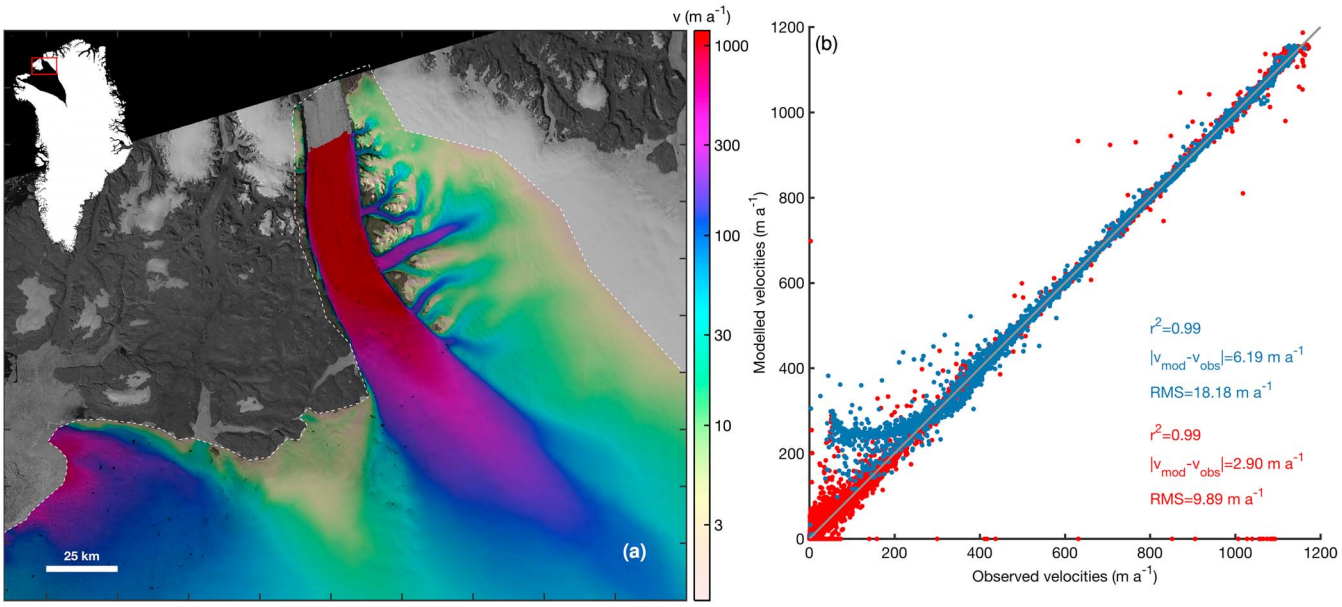

Figure 3. (a) Modeled surface velocities for the *init* experiment. Background image is a mosaiced Landsat ETM+ and RADARSAT imagery from the years 1999 to 2002 (Howat et al., 2014). The inset shows the model domain and the zoom area in black and red, respectively. The white dashed line delineates the model domain in the zoom area. (b) Scatter plot of modeled and observed velocities for the *init* experiment. The red and blue dots represent velocities from the grounded and floating regions, respectively. The gray lines define the identity.

where η is the ice viscosity, H the local ice thickness, z_s the upper surface elevation, and $\tau_b = (\tau_{b,x}, \tau_{b,y})$ the basal drag. Vertical velocity, w, is recovered from incompressibility

$$\frac{\partial u}{\partial x} + \frac{\partial v}{\partial y} + \frac{\partial w}{\partial z} = 0. \tag{4}$$

As we use the SSA equations and perform perturbations experiments of short timescales, we do not perform a thermo-mechanical coupling but prescribe the bulk ice rigidity factor, B, in Glen's flow law that enters the ice viscosity η.

For the dynamic model, we apply water pressure at the calving front of PGs floating tongue and of marine-terminating glaciers. Observed surface velocities are prescribed at the ice divides. A traction-free boundary condition is imposed at the ice/air interface. At the ice base sliding is allowed everywhere, and the basal drag is written using Coulomb friction

$$\boldsymbol{\tau}_b = -k^2 N \mathbf{v}_b, \tag{5}$$

where $\mathbf{v}_b = (u_{b,x}, v_{b,y})$ is the basal velocity vector tangential to the glacier base and k^2 a scalar field representing the basal friction coefficient. The effective pressure is defined as $N = \varrho_i g H + \varrho_w g \min(z_b,0)$, where z_b is the glacier base. Instead of prescribing a boundary condition directly at the lateral margins of the floating tongue (where it is in contact with the side walls), we slightly enlarge the modeling domain toward the grounded part. At this shifted margin we prescribe a Dirichlet condition that does neither affect the floating tongue nor the deformation of a shear margin.

We perform time-dependent model runs, which solves the ice dynamic equations independent of time (equations (2) and (3)), but the simulated ice thickness change consists of the divergence of the volume flux, plus surface and basal mass balance

$$\frac{\partial H}{\partial t} + \nabla \cdot H \mathbf{v}_h = \dot{M}_s + \dot{M}_b. \tag{6}$$

The surface mass balance ($\dot{M}_s$) applied here is a multiyear mean from the downscaled RACMO2.3 data set between 1979 and 2015 (Noël et al., 2016). The basal mass balance ($\dot{M}_b$) of the floating tongue is taken from this study (Figure 1 and section 2.4). As the observations of the grounding line migration exhibit only minor variations in extent of the floating part, we do not need to extrapolate our basal melt rate field. At the base of grounded ice no melting is assumed. Other than equation (1), the equation here is defined in an Eulerian framework.

The calving front motion is solved by a level set method, which tracks the ice front according to the kinematic calving front condition (Bondzio et al., 2016; 2017)

$$\mathbf{w}_{\mathrm{cf}} = \mathbf{v}_h - (c^{\perp} + M^{\perp}_{\mathrm{cf}})\mathbf{n}_{\mathrm{cf}}, \tag{7}$$

where $\mathbf{w}_{\mathrm{cf}}$ is the horizontal calving front velocity vector, $c^{\perp}$ the calving rate in the normal direction, M_{cf} the frontal melt rate, and $\mathbf{n}_{\mathrm{cf}}$ the unit normal vector at the calving front pointing outward of the ice domain. The level set function is obtained from a Hamilton Jacobi-type partial differential equation that is discretized in an area exceeding the ice domain and evaluated for the level set to become $c^{\perp} + M^{\perp}_{\mathrm{cf}}$ (Bondzio et al., 2016). Here $c^{\perp} + M^{\perp}_{\mathrm{cf}}$ is obtained from remote sensing data (shown above), and hence, we simulate the response of PG to variations of the ice front motion.

The simulation setups comprise one steady state and several transient simulations. The former is dedicated to retrieve the initial ice flow in January 2012, prior to the calving event in July 2012, and serves then as input for the transient runs. Starting from the initial state in January 2012, the transient simulations pass the calving event and extend until January 2017. Additionally, we investigate the effect of a calving event that takes place arbitrarily in summer 2018. Before this experiment, we investigate the effect of mechanical weakening in the observable fractures which likely determine the future terminus outline. Specifically, we conduct the following simulations:

1. *init:* initialize and reproduce the flow of PG before the 2012 calving event,
2. *ctrl:* unforced control run to account for model drift,
3. *calv2012:* response to the calving event in 2012,
4. *fracture:* response to newly developed fractures,
5. *potential calv:* response to an anticipated calving event that occurs arbitrarily in summer 2018.

According to the Courant-Friedrich-Lewy condition, a time step of 0.005 year is required. The very small time step is due to the high resolution in the fracture zones. Although only one experiment accounts for these zones, all experiments are run on the same mesh to ensure comparability.

3.2. Results of Modeling Experiments

Before starting our perturbation experiments, we need to find a reasonable initial state that matches the stress regime of the pre-2012 calving state. For this *init* experiment, we engage data assimilation techniques relying on Ice Sheet System Model's inversion capabilities to constrain unknown or poorly constrained parameters. Specifically, in this study, the inversion approach infers the basal friction coefficient, k^2, in the grounded part and the bulk ice rigidity, B, in the floating part by minimizing a cost function that measures the misfit between observed and modeled horizontal velocities. The cost function is composed of two terms which fit the velocities in fast- and slow-moving areas. A third term is a Tikhonov regularization to avoid oscillations. For the observational data set, we use the precalving ice velocities from January 2012 from this study nested into the MEaSUREs data set (Joughin et al., 2010; Joughin, Smith, Howat, & Scambos, 2016). A constant bulk ice rigidity corresponding to −5°C is prescribed for grounded ice. This relatively warm value compared to the ice surface accounts for shearing in the basal layers that is not intrinsically simulated. The friction coefficient is zero for floating ice. As the inversions for the friction coefficient and the rheology are performed in subsequent runs, we iterate over both to ensure a smooth transition in the overlapping area (the grounding zone). In doing so, we are able to reproduce the pre-2012 calving ice flow of PG with sufficient accuracy in both the grounded and floating parts (Figure 3). When compared to our remote sensing estimates, we obtained root-mean-square errors of $\mathrm{RMS}_{\mathrm{grounded}} = 9.89\ \mathrm{m\ a^{-1}}$ and $\mathrm{RMS}_{\mathrm{floating}} = 18.18\ \mathrm{m\ a^{-1}}$ for the grounded part and the floating part, respectively (Figure 3b). The initial grounding line flux is estimated with 10.55 Gt $\mathrm{a^{-1}}$ and is roughly in accordance with the mean value of 9.82 ± 0.47 Gt $\mathrm{a^{-1}}$ provided by Wilson et al. (2017) for the period between 2011 and 2015 (We used an ice density of 910 kg $\mathrm{m^{-3}}$ to convert their value to gigatons per year).

The retrieved basal friction coefficient, k^2, and the bulk ice rigidity, B, are shown in Figure 4. The basal friction coefficient reveals a distribution that correlates with the flow magnitude: low values in areas of fast flow and higher values in areas with slow flow. Within the ice stream, the friction coefficient does not vary substantially. In contrast, the bulk ice rigidity reveals a more complex pattern. This is because the inverse solution contains information about both the temperature of the ice and any areas of softened or weakened ice. The inversion for the bulk ice rigidity factor, in particular, produces nonphysically high and low values in terms of ice shelf bulk temperatures. Generally, low rigidity is found parallel to the fjord sidewalls

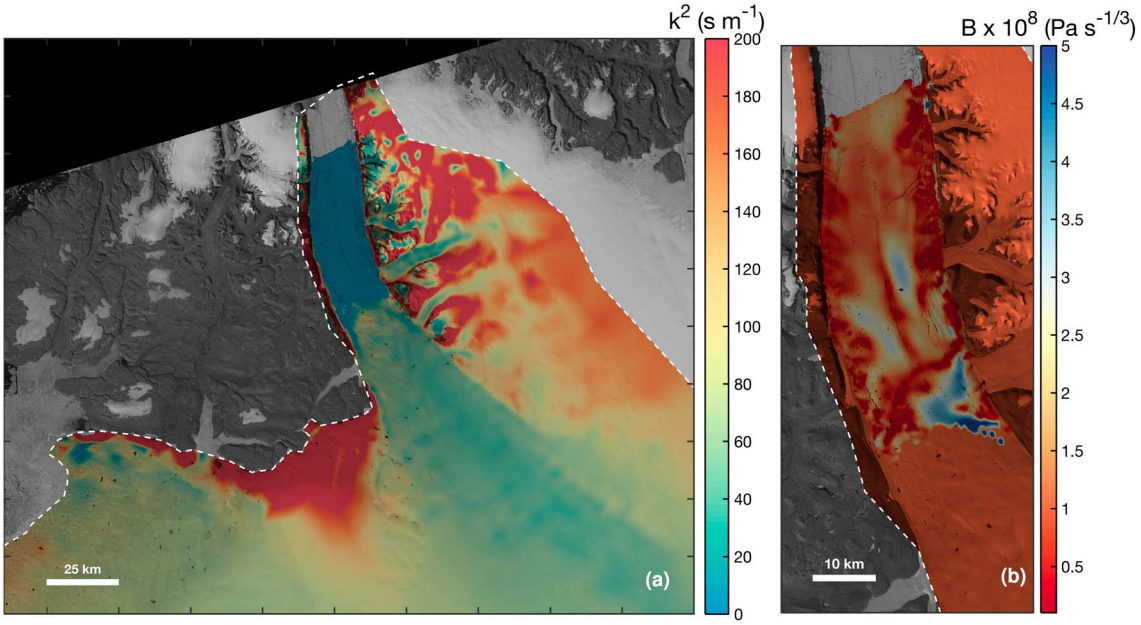

Figure 4. Inferred values from the *init* experiment. (a) Basal friction coefficient k^2; high values (red) represent high friction and low values (blue) less friction. (b) Bulk ice rigidity B; high values (blue) represent stiff ice and low values (dark red) soft ice.

(Figure 4b). This weakening or fracturing coincides with the shear margins in that area, and consequently, the simulated velocity field of PGs floating tongue reveals the continuously high velocities in the central part and the sharp drop toward the fjord sidewalls. From the inversion, stiff ice is primarily found in the upper part of the floating tongue, particularly in the grounding zone.

In the first transient model experiment, we investigate the effect of ongoing dynamic and geometric changes that are related to the initialization. A shortcoming of the performed initialization is that a fixed initial ice sheet geometry causes a model drift when imposing the ice thickness equation. This is a result from using an ice sheet that is not in equilibrium with the applied surface and basal mass balance and ice flux divergence. In an unforced relaxation run the velocities have increased up to 1,200 m a^{-1} in the center of the floating tongue after 5 years and exceeded the magnitude of the 2012 calving event ($RMS_{grounded} = 94.18$ m a^{-1} and $RMS_{floating} = 77.35$ m a^{-1}). Therefore, we utilize the local ice thickness imbalance once the ice sheet is released from its fixed topography from a 1-year unforced relaxation run. The resulting $\partial H/\partial t$ is subtracted as a surface and basal mass balance correction for the further runs (similar as in Goelzer et al., 2013; Price et al., 2011). In doing so, a *ctrl* run without any perturbation in the forcing fields and with a nonmoving calving front, that is, $\mathbf{w}_{cf} = \left(c^{\perp} + M_{cf}^{\perp}\right) \quad \mathbf{n}_{cf}$ in equation (7), exhibits almost no velocity variations over the 5-year simulation period. That is reflected by the RMS errors that remain almost unchanged compared to the *init* experiment ($RMS_{grounded} = 9.72$ m a^{-1}, $RMS_{floating} = 19.10$ m a^{-1} and see also black dashed line for the *ctrl* experiment in Figure 5).

In the next *calv2012* experiment, we investigate the response of PG to the calving event that took place on July 2012. In order to simulate an immediate calving event, we manually prescribe an extremely high calving rate ($c^{\perp} + M_{cf}^{\perp}$) up to 50 km a^{-1} at the ice front until the ice front position observed in January 2013 is reached. Afterward, the calving rate is set to zero. The iceberg break off appears instantaneously within one time step in the numerical model. In response to the loss in frontal area, the simulated velocity field reveals the satellite-derived speedup of about 50 m a^{-1} (Figure 5a). The main difference between the observations and the model output occurs downstream of the grounding zone (distance around 0–20 km), where the simulation does not fully reproduce the observed speedup. Nevertheless, the flux over the grounding line is increased by 0.09 Gt a^{-1}. After the calving event, the position of the calving front readvances, while the simulated velocities remain faster than the pre-2012 calving velocities; over time the velocities decrease slightly. This is due to the fact that the inferred rheology from the inversion is maintained fixed in space and time, and the simulation aims to approach the pre-2012 calving state.

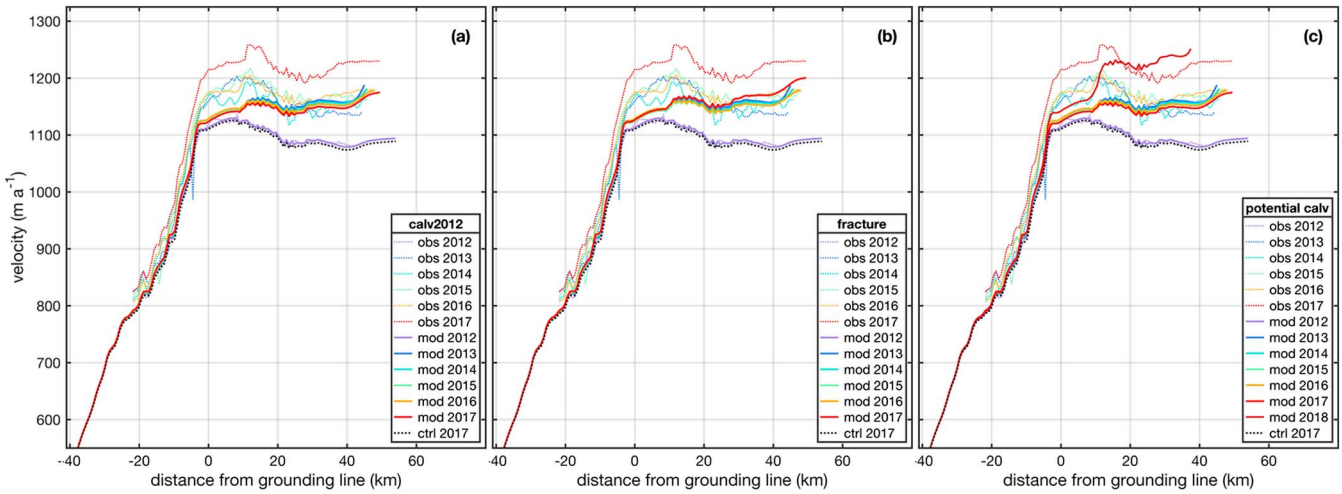

Figure 5. Time series of surface velocities along the central flowline shown in Figure 1 for the *calv2012* experiment (a), for the *fracture* experiment (b), and for the *potential calv* experiment in 2018 (c). Dashed and solid lines indicate observed and modeled velocities, respectively.

Most evidently, the speedup observed in winter 2016/2017 is not reproduced by this scenario. So far, no further breakup has occurred at PG, but newly developing fractures close to the terminus have been observed in summer 2017 (Figure S3). This features might indicate an onset of decoupling of the frontal part of the floating tongue and hence a reduced back stress exerted on the floating tongue. Following the approach of Humbert et al. (2009), we mimic the fractures by reducing the viscosity of about 90% in these areas after the winter 2016/2017. Figure 5b shows the response of the velocity of PG to this *fracture* scenario. In this experiment, the velocity increase after the July 2012 calving event remains unaltered, but velocities at the front of the ice shelf slightly increase in summer 2017. The speedup of approximately 20 m a^{-1} is smaller than the observed variations (around 40–80 m a^{-1}). The flux over the grounding line remains constant.

In a series of major calving events that occurred at PG during the last decade, a new calving event could be expected in the near future. In order to estimate the response of PG to a new calving event, we set a date for this event arbitrarily to July 2018. The estimated frontal position is shown as a red line in Figure 1b and is based on the newly developing fractures in the frontal part (Figure S3). We rerun the *calv2012* experiment by using the inversion inferred rheology until the assumed July 2018 frontal position is reached. Under this next *potential calv* scenario, PG experiences a further calving front retreat of about 12 km accompanied by a further speedup (Figure 5c). Velocities in the frontal part reach 1,240 m a^{-1}, and the speedup between the post-2012 and the potential calving events is of similar magnitude compared to the 2012 breakoff event. Similar to the previous calving experiment, a small speedup at the grounding zone is simulated but smaller than the observed magnitude in December 2016. The flux over the grounding line additionally increases by 0.13 Gt a^{-1}.

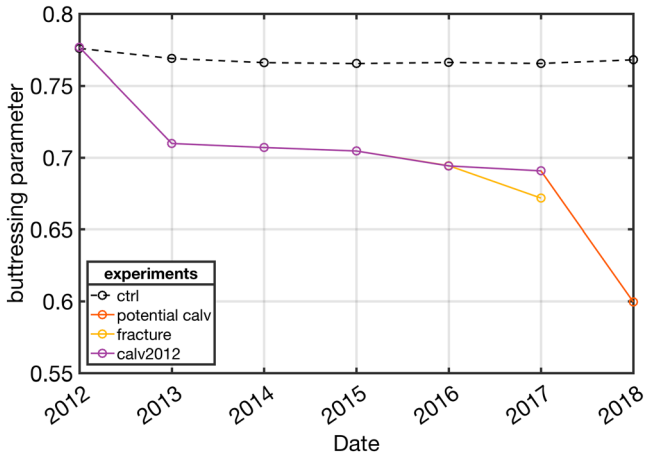

Figure 6. Spatial mean buttressing parameter f according to equation (18) in Borstad et al. (2013) at certain times for all conducted transient experiments. A value of $f = 1$ represent a fully buttressed ice shelf while a value of $f = 0$ an unbuttressed ice shelf. Please note that the lines for the experiments *calv2012, fracture* and *potential calv* are similar until 2016.

As an estimation of the back stress exerted by the floating tongue, we calculate a normalized buttressing parameter, f, following Borstad et al., 2013 (2013, equation 18 without the partition of bulk ice rigidity into the damage and temperature dependent part). Besides geometric and rheologic parameters the buttressing parameter is calculated from contributions of lateral and shear strain rates ($\dot{\varepsilon}_{xx}$, $\dot{\varepsilon}_{yy}$ and $\dot{\varepsilon}_{xy}$). In the end, a value of $f = 0$ corresponds to an un-buttressed ice shelf while a value of $f = 1$ represents a fully buttressed ice shelf. For all experiments, we calculate the spatial mean buttressing parameter over the floating tongue (Figure 6). The control run shows a relatively constant level of buttressing over the entire time period, while for the calving experiments, the buttressing is reduced by the calving events on Jul 2012 and Jul 2018. The fracture experiment leads to a slight reduction in buttressing. The spatial distribution of the buttressing parameter is illustrated in Figure 7. After

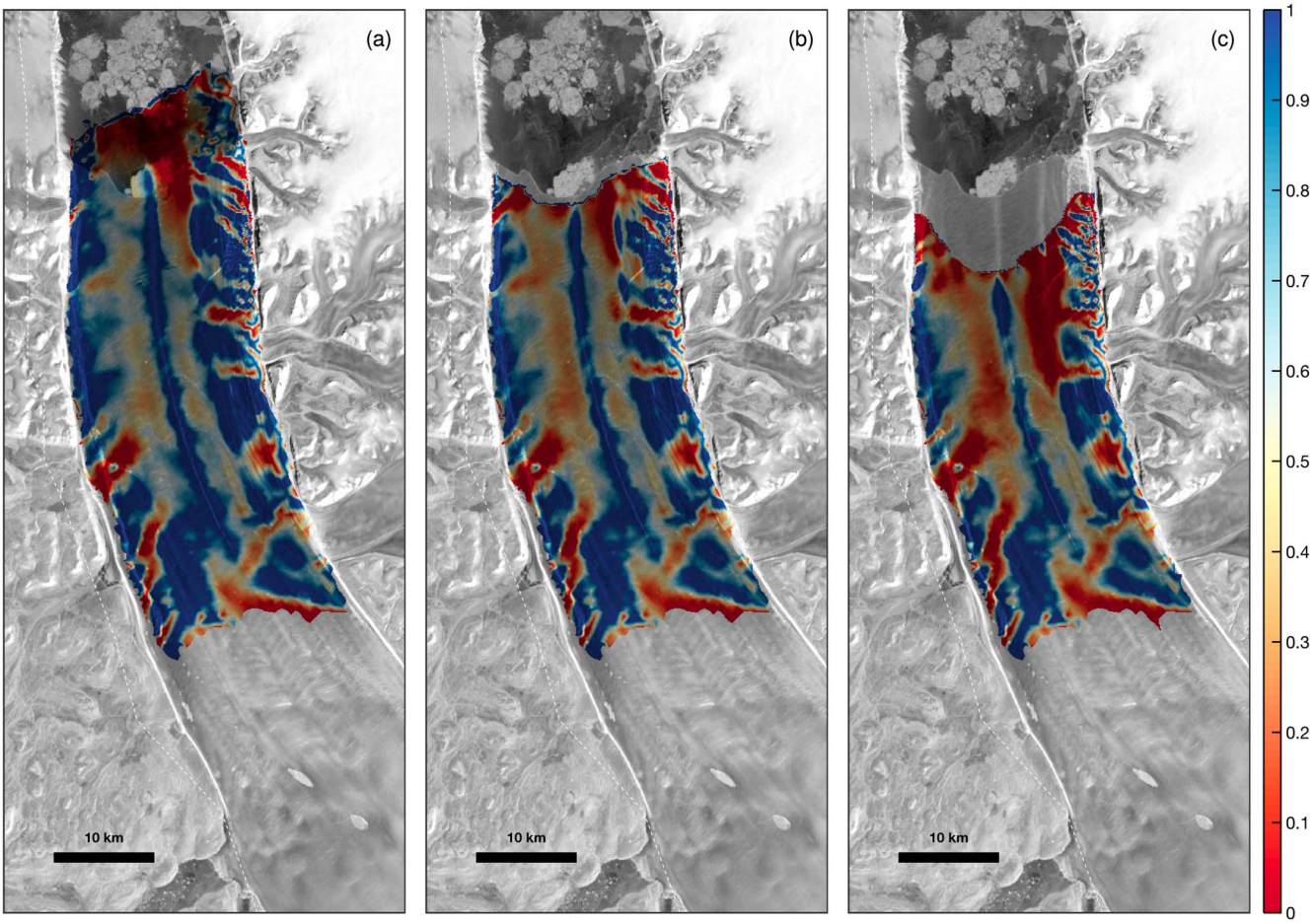

Figure 7. Buttressing parameter f according to equation (18) in Borstad et al. (2013) for the *init* experiment (a), for the *calv2012* experiment (b), and for the *potential calv* experiment (c). Background image is a mosaiced RADARSAT-1 imagery from the years 2012 to 2013 (Joughin, 2015; Joughin, Smith, Howat, Moon et al., 2016).

the 2012 calving event the buttressing effect decreases up to ~25 km upstream of the western terminus and up to ~15 km of the eastern terminus. The subsequent calving event causes further reduction in buttressing which is most pronounced in the northern half of the remaining floating tongue. The area downstream the grounding line remains basically unchanged.

4. Discussion

The time series of observed surface velocities highlights the interannual speedup of PG after the major calving event of July 2012. After a phase of relatively constant velocities, a second speedup of similar magnitude occurred between February 2016 and December 2016. With an average acceleration of 10% between January/February 2012 and December 2016 the observed speedups are only minor compared to the seasonal acceleration of ~25% in summer (Nick et al., 2012) and to the interannual speedup of several other marine-terminating outlet glaciers in Greenland (e.g., Howat et al., 2005; Joughin et al., 2014; Mouginot et al., 2015). Nonetheless, the observed speedups are detectable from the remotely sensed time series and might reflect the start of dynamic changes at PG. This finding is further supported by variations in grounding line location based on SAR interferometry. However, as already pointed out by Hogg et al. (2016), these estimates should be handled with care, as the amplitude of variation can exceed the average variation by up to one order of magnitude, especially in the eastern part of PG.

Our modeling experiments suggest that the July 2012 calving event is a potential trigger for the first speedup. Also, the more recent speedup could be partly connected to newly developing fractures, which propagate from the eastern and western fjord walls to the center of the floating ice tongue. Basically, this experiment

captures the increasing velocity trend, but the actual magnitude of the speedup is still off. One reason for this difference could be that the effect of mechanical weakening extends beyond the immediate regions around the active fractures visible in the satellite imagery (Figure S3). Although the 2016 speedup does not directly correlate with an observed calving event, we show that the developing fractures could already mechanically decouple the ice from the main floating tongue by reducing the buttressing exerted on the floating tongue. If this is the case, the detachment of the frontal part downstream the observed fractures will not cause a further speedup above the winter 2016/2017 level.

Compared to the fracture experiment, the recently observed speedup is better reproduced by an arbitrary calving event. In general, the conducted calving experiments can reproduce the observed speedup in the frontal part but fail to fully reproduce the observed speedup until ~ 20 km downstream the grounding line. We attribute this underestimation of the speedup to the inversion inferred ice rheology of the floating tongue that reflects the pre-2012 calving state and remains unaltered during the perturbation experiments. The July 2012 calving event and the associated speedup may have trigger new weak zones further upstream the calving front. As possible feedback of mechanical weakening or fracturing in the shear zones the floating tongue could experience a reduction of the lateral drag and hence in further acceleration. This feedback mechanism is confirmed by the fracture experiment, where we see that manually weakening added at the observable fractures causes a minor speedup. The numerical model does not capture this positive feedback as we rely on an inversion-based model approach where the rheology is not able to adjust to the calving events and still reflect the initial state situation. Another reason for the models failure to capture the speedup near the grounding line could be that the model is not capturing grounding line migration well. Although we show that grounding line migration is minimal, a little retreat could affect the flow field.

In contrast to the minor response of PG to the major calving event in Aug 2010, the 2012 calving event produced a detectable glacier speedup (Figures 2 and S2). By employing a 2-D flowline model, Nick et al. (2012) investigated the 2010 calving event. They successfully reproduced the pre-2010 velocity field and geometry by introducing a lateral drag coefficient in the rheology. From this setup, they simulated the 2010 calving event and found that the ice flow reacts insensitive to this calving event. They concluded, that this is a direct consequence of the very low along-flow resistive stresses for the front part of the ice shelf, resulting from the limited attachment to the fjord walls (Nick et al., 2012). Subsequently to the 2010 calving event, Nick et al. (2012) performed an arbitrary calving experiment with a retreat of 20 km after 4 years. This experiment roughly represents the actual terminus retreat in 2012 and results in a larger velocity increase and ice discharge than in their 2010 calving experiment. They concluded that the enhanced sensitivity to calving could be explained by the greater loss of lateral buttressing as the ice shelf is thicker and closer to the grounding line. Therefore, our results are in line with Nick et al. (2012) and confirm that the trend of ice flow acceleration is related to the attachment of the ice tongue to the fjord sidewalls. Given the two different modeling approaches, 2-D flowline model vs 2-D plan view model, the similarity in results is impressive. Based on both studies, we can infer if major calving events occur more frequently and the calving front continues to retreat, PG will likely experience enhanced acceleration.

The study by Nick et al. (2012) demonstrates that seasonal speedup at PG is mainly driven by meltwater lubrication and that sub-shelf ocean melt controls the future stability. Subshelf ocean melt rates, derived from a Lagrangian thickness change field, showed the highest melt near the grounding zone and along several basal channels, highlighting a high spatial variability. Our basal melt rates compare well (both in magnitude and spatial distribution) to previous studies based on remote sensing and in situ measurements (Cai et al., 2017; Dutrieux et al., 2014; Wilson et al., 2017). Minor changes in basal melt rates are supported by hydrographic observations in the Petermann Fjord (Heuzé et al., 2017; Johnson et al., 2011). The latter studies hypothesize that cold and low-salinity Winter Water from Nares Strait protrudes under the floating ice tongue, limiting enhanced basal melting to water depths of 150 m to >1,000 m. Until now, this could explain the similar precalving and postcalving melt water concentrations measured in Petermann Fjord (Heuzé et al., 2017). However, the anticipated next calving event could set larger parts of the ice base in the new terminus region to deeper water depth, making the entire ice tongue more vulnerable to increased ocean warming.

5. Conclusions

In this study, we combine observations and numerical ice flow modeling to investigate how various calving events impact the dynamics of PG. Contrary to the 2010 calving event, which did not result in a significant speedup of Petermann Glacier, we show that the combination of both the 2012 and a subsequent calving event lead to a 10% speedup of ice velocities. Compared to a seasonal acceleration of ~25%, this is only minor, but if the trend of a retreating calving front continues, PG is likely to further accelerate in the future. We attribute this to a loss of buttressing caused by the retreat further upstream and a subsequent loss of friction with the fjords walls. The impact of calving on the simulated ice flow is limited by the treatment of the floating tongues ice rheology and inclusion of observable fracture zones. The inversion inferred rheology is treated fixed in time and space, as a consequence whether changing weak/stiff zones nor developing fractures are considered. However, the observed speedup in 2016 suggests that the ice in the frontal part is already detached from the stabilizing fjord walls. Provided that the ice breaks in the newly developed fracture zone, no additional speedup is assumed for the next calving event.

Acknowledgments

M. R. was funded by the Helmholtz Alliance Climate Initiative (REKLIM). N. N. received funding from the European Unions Horizon 2020 research and innovation programme under grant agreement 689443 via project iCUPE (Integrative and Comprehensive Understanding on Polar Environments). S. B was financially supported by the FRS-FNRS (Fonds de la Recherche Scientifique) and Belgian Federal Science Policy Office (MIMO project, SR/00/336). We thank two anonymous reviewers for their helpful comments which greatly improved the quality of the manuscript. We are grateful for the RACMO data provided by Peter Kuipers Munneke and Brice Noël (both IMAU). We would like to thank Malte Thoma, Natalja Rakowsky, and Vadym Aizinger for maintaining excellent computing facilities even under technically challenging circumstances at AWI. We also would like to thank the general support of the ISSM team. Operation IceBridge laser altimeter measurements were provided by the National Snow and Ice Data Center. TanDEM-X and TerraSAR-X data were made available through German Aerospace Center proposals GLAC0267, GLAC7208, and HYD2059. Remotely sensed surface velocities, Lagrangian basal melt rates, terminus positions, grounding lines as well as modeling results are available via the PANGAEA (www.pangaea.de) database (https://doi.pangaea.de/10.1594/PANGAEA.896907).

References

Bamber, J. L., Griggs, J. A., Hurkmans, R. T. W. L., Dowdeswell, J. A., Gogineni, S. P., Howat, I., et al. (2013). A new bed elevation dataset for Greenland. *The Cryosphere*, *7*(2), 499–510. https://doi.org/10.5194/tc-7-499-2013

Berger, S., Drews, R., Helm, V., Sun, S., & Pattyn, F. (2017). Detecting high spatial variability of ice shelf basal mass balance, Roi Baudouin Ice Shelf, Antarctica. *The Cryosphere*, *11*(6), 2675–2690. https://doi.org/10.5194/tc-11-2675-2017

Bondzio, J. H., Morlighem, M., Seroussi, H., Kleiner, T., Rückamp, M., Mouginot, J., et al. (2017). The mechanisms behind jakobshavn Isbræ's acceleration and mass loss: A 3-D thermomechanical model study. *Geophysical Research Letters*, *44*, 6252–6260. https://doi.org/10.1002/2017GL073309

Bondzio, J. H., Seroussi, H., Morlighem, M., Kleiner, T., Rückamp, M., Humbert, A., & Larour, E. Y. (2016). Modelling calving front dynamics using a level-set method: Application to Jakobshavn Isbræ, West Greenland. *The Cryosphere*, *10*(2), 497–510. https://doi.org/10.5194/tc-10-497-2016

Borstad, C. P., Rignot, E., Mouginot, J., & Schodlok, M. P. (2013). Creep deformation and buttressing capacity of damaged ice shelves: Theory and application to Larsen C ice shelf. *The Cryosphere*, *7*(6), 1931–1947. https://doi.org/10.5194/tc-7-1931-2013

Cai, C., Rignot, E., Menemenlis, D., & Nakayama, Y. (2017). Observations and modeling of ocean-induced melt beneath Petermann Glacier ice shelf in northwestern Greenland. *Geophysical Research Letters*, *44*, 8396–8403. https://doi.org/10.1002/2017GL073711

Dutrieux, P., Stewart, C., Jenkins, A., Nicholls, K. W., Corr, HughF. J., Rignot, E., & Steffen, K. (2014). Basal terraces on melting ice shelves. *Geophysical Research Letters*, *41*, 5506–5513. https://doi.org/10.1002/2014GL060618

Falkner, K. K., Melling, H., Münchow, A. M., Box, J. E., Wohlleben, T., Johnson, H. L., et al. (2011). Context for the recent massive Petermann Glacier calving event. *Eos, Transactions American Geophysical Union*, *92*(14), 117–118. https://doi.org/10.1029/2011EO140001

Goelzer, H., Huybrechts, P., Fürst, J. J., Nick, F. M., Andersen, M. L., Edwards, T. L., et al. (2013). Sensitivity of Greenland ice sheet projections to model formulations. *Journal of Glaciology*, *59*(216), 733–749. https://doi.org/10.3189/2013JoG12J182

Heuzé, C., Wåhlin, A., Johnson, H. L., & Münchow, A. (2017). Pathways of meltwater export from Petermann Glacier, Greenland. *Journal of Physical Oceanography*, *47*(2), 405–418. https://doi.org/10.1175/JPO-D-16-0161.1

Hogg, A. E., Shepherd, A., Gourmelen, N., & Engdahl, M. (2016). Grounding line migration from 1992 to 2011 on Petermann Glacier, North-West Greenland. *Journal of Glaciology*, *62*(236), 1104–1114. https://doi.org/10.1017/jog.2016.83

Howat, I. M., Joughin, I., Tulaczyk, S., & Gogineni, S. (2005). Rapid retreat and acceleration of Helheim Glacier, east Greenland. *Geophysical Research Letters*, *32*, 4. https://doi.org/10.1029/2005GL024737

Howat, I. M., Negrete, A., & Smith, B. E. (2014). The Greenland ice mapping project (GIMP) land classification and surface elevation data sets. *The Cryosphere*, *8*(4), 1509–1518. https://doi.org/10.5194/tc-8-1509-2014

Humbert, A., Kleiner, T., Mohrholz, C. O., Oelke, C., Greve, R., & Lange, M. A. (2009). A comparative modeling study of the brunt ice shelf/Stancomb-Wills Ice Tongue system, East Antarctica. *Journal of Glaciology*, *55*(189), 53–65. https://doi.org/10.3189/002214309788608949

Johnson, H. L., Münchow, A., Falkner, K. K., & Melling, H. (2011). Ocean circulation and properties in Petermann fjord, Greenland. *Journal of Geophysical Research*, *116*, C01003. https://doi.org/10.1029/2010JC006519

Joughin, I. (2015). *MEaSUREs Greenland Ice Sheet Mosaics from SAR Data, Version 1*. Boulder, CO: NASA National Snow and Ice Data Center Distributed Active Archive Center. https://doi.org/10.5067/6187DQUL3FR5

Joughin, I., & Moon, T. (2015). *MEaSUREs Annual Greenland Outlet Glacier Terminus Positions from Sar Mosaics*. Boulder, CO: NASA National Snow and Ice Data Center Distributed Active Archive Center. https://doi.org/10.5067/DC0MLBOCL3EL

Joughin, I., Shean, D. E., Smith, B. E., & Dutrieux, P. (2016). Grounding line variability and subglacial lake drainage on Pine Island Glacier, Antarctica. *Geophysical Research Letters*, *43*, 9093–9102. https://doi.org/10.1002/2016GL070259

Joughin, I., Smith, B. E., Howat, I. M., Moon, T., & Scambos, T. A. (2016). A SAR record of early 21st century change in Greenland. *Journal of Glaciology*, *62*(231), 62–71. https://doi.org/10.1017/jog.2016.10

Joughin, I., Smith, B., Howat, I., & Scambos, T. (2015). *MEaSUREs Greenland Ice Sheet Velocity Map from InSAR Data, Version 2, updated 2017*. Boulder, CO: NASA National Snow and Ice Data Center Distributed Active Archive Center. https://doi.org/10.5067/OC7B04ZM9G6Q

Joughin, I., Smith, B., Howat, I., & Scambos, T. (2016). *MEaSUREs Multi-Year Greenland Ice Sheet Velocity Mosaic, version 1.*Boulder, CO: NASA National Snow and Ice Data Center Distributed Active Archive Center.

Joughin, I., Smith, B., Howat, I., Scambos, T., & Moon, T. (2010). Greenland flow variability from ice-sheet-wide velocity mapping. *Journal of Glaciology*, *56*(197), 415–430. https://doi.org/10.3189/002214310792447734

Joughin, I., Smith, B. E., Shean, D. E., & Floricioiu, D. (2014). Brief communication: Further summer speedup of Jakobshavn Isbræ. *The Cryosphere*, *8*(1), 209–214. https://doi.org/10.5194/tc-8-209-2014

Kuipers Munneke, P., Ligtenberg, S. R. M., Noël, B. P. Y., Howat, I. M., Box, J. E., Mosley-Thompson, E., et al. (2015). Elevation change of the Greenland Ice Sheet due to surface mass balance and firn processes, 1960-2014. *The Cryosphere*, *9*(6), 2009–2025. https://doi.org/10.5194/tc-9-2009-2015

Larour, E., Seroussi, H., Morlighem, M., & Rignot, E. (2012). Continental scale, high order, high spatial resolution, ice sheet modeling using the ice sheet system model (ISSM). *Journal of Geophysical Research*, *117*, F01022. https://doi.org/10.1029/2011JF002140

Lüttig, C., Neckel, N., & Humbert, A. (2017). A combined approach for filtering ice surface velocity fields derived from remote sensing methods. *Remote Sensing*, *9*(10), 23. https://doi.org/10.3390/RS9101062

MacAyeal, D. R. (1989). Large-scale ice flow over a viscous basal sediment: Theory and application to ice stream b, Antarctica. *Journal of Geophysical Research*, *94*(B4), 4071–4087. https://doi.org/10.1029/JB094iB04p04071

Marsh, O. J., Rack, W., Floricioiu, D., Golledge, N. R., & Lawson, W. (2013). Tidally induced velocity variations of the Beardmore glacier, Antarctica, and their representation in satellite measurements of ice velocity. *The Cryosphere*, *7*(5), 1375–1384. https://doi.org/10.5194/tc-7-1375-2013

Moon, T., & Joughin, I. (2008). Changes in ice front position on Greenland's outlet glaciers from 1992 to 2007. *Journal of Geophysical Research*, *113*, F02022. https://doi.org/10.1029/2007JF000927

Moon, T., Joughin, I., & Smith, B. (2015). Seasonal to multiyear variability of glacier surface velocity, terminus position, and sea ice/ice mélange in northwest Greenland. *Journal of Geophysical Research: Earth Surface*, *120*, 818–833. https://doi.org/10.1002/2015JF003494

Morlighem, M., Rignot, E., Mouginot, J., Seroussi, H., & Larour, E. (2014). Deeply incised submarine glacial valleys beneath the Greenland ice sheet. *Nature Geoscience*, *7*, 418–422. https://doi.org/10.1038/ngeo2167

Mouginot, J., Rignot, E., Scheuchl, B., Fenty, I., Khazendar, A., Morlighem, M., et al. (2015). Fast retreat of Zachariæ Isstrøm, northeast Greenland. *Science*, *350*(6266), 1357–1361. https://doi.org/10.1126/science.aac7111

Münchow, A., Padman, L., & Fricker, H. A. (2014). Interannual changes of the floating ice shelf of Petermann Gletscher, North Greenland, from 2000 to 2012. *Journal of Glaciology*, *60*(221), 489–499. https://doi.org/10.3189/2014JoG13J135

Münchow, Andreas, Padman, Laurie, Washam, Peter, & Nicholls, Keith (2016). The ice shelf of Petermann Gletscher, North Greenland, and its connection to the Arctic and Atlantic oceans. *Oceanography*, *29*(4), 84–95. https://doi.org/10.5670/oceanog.2016.101

Neckel, N., Braun, A., Kropáček, J., & Hochschild, V. (2013). Recent mass balance of the Purogangri ice cap, central Tibetan Plateau, by means of differential X-band SAR interferometry. *The Cryosphere*, *7*(5), 1623–1633. https://doi.org/10.5194/tc-7-1623-2013

Nick, F. M., Luckman, A., Vieli, A., Van Der Veen, C. J., Van As, D., Van De Wal, R. S. W., et al. (2012). The response of Petermann Glacier, Greenland, to large calving events, and its future stability in the context of atmospheric and oceanic warming. *Journal of Glaciology*, *58*(208), 229–239. https://doi.org/10.3189/2012JoG11J242

Noël, B., van de Berg, W. J., Machguth, H., Lhermitte, S., Howat, I., Fettweis, X., & van den Broeke, M. R. (2016). A daily, 1 km resolution data set of downscaled Greenland ice sheet surface mass balance (1958–2015). *The Cryosphere*, *10*(5), 2361–2377. https://doi.org/10.5194/tc-10-2361-2016

Padman, L., & Erofeeva, S. (2004). A barotropic inverse tidal model for the Arctic Ocean. *Geophysical Research Letters*, *31*, 4. https://doi.org/10.1029/2003GL019003

Price, S. F., Payne, A. J., Howat, I. M., & Smith, B. E. (2011). Committed sea-level rise for the next century from Greenland ice sheet dynamics during the past decade. *Proceedings of the National Academy of Sciences*, *108*(22), 8978–8983. https://doi.org/10.1073/pnas.1017313108

Rignot, E., Mouginot, J., & Scheuchl, B. (2011). Antarctic grounding line mapping from differential satellite radar interferometry. *Geophysical Research Letters*, *38*, L10504. https://doi.org/10.1029/2011GL047109

Rignot, E., & Steffen, K. (2008). Channelized bottom melting and stability of floating ice shelves. *Geophysical Research Letters*, *35*, L02503. https://doi.org/10.1029/2007GL031765

Seehaus, T., Marinsek, S., Helm, V., Skvarca, P., & Braun, M. (2015). Changes in ice dynamics, elevation and mass discharge of Dinsmoor-Bombardier-Edgeworth glacier system, Antarctic peninsula. *Earth and Planetary Science Letters*, *427*, 125–135. https://doi.org/10.1016/j.epsl.2015.06.047

Strozzi, T., Luckman, A., Murray, T., Wegmuller, U., & Werner, C. (2002). Glacier motion estimation using SAR offset-tracking procedures. *IEEE Transactions on Geoscience and Remote Sensing*, *40*(11), 2384–2391. https://doi.org/10.1109/tgrs.2002.805079

Studinger, M. S. (2014). *Updated 2017 IceBridge ATM L2 Icessn Elevation, Slope, and Roughness, Version 2*. Boulder, CO: NASA National Snow and Ice Data Center Distributed Active Archive Center. https://doi.org/10.5067/CPRXXK3F39RV

Wessel, B., Bertram, A., Gruber, A., Bemm, S., & Dech, S. (2016). A new high-resolution elevation model of Greenland derived from TanDEM-X, *XXIII ISPRS congress* (Vol. III-7, pp. 9–16). Retrieved from https://elib.dlr.de/107017/

Wilson, N., Straneo, F., & Heimbach, P. (2017). Satellite-derived submarine melt rates and mass balance (2011–2015) for Greenland's largest remaining ice tongues. *The Cryosphere*, *11*(6), 2773–2782. https://doi.org/10.5194/tc-11-2773-2017

Zwally, H. J., Giovinetto, M. B., Beckley, M. A., & Saba, J. L. (2012). Antarctic and greenland drainage systems. GSFC Cryospheric Sciences Laboratory. Retrieved from https://icesat4.gsfc.nasa.gov/cryo_data/ant_grn_drainage_systems.php